RSC Advances

PAPER

View Article Online
View Journal | View Issue

Cite this: *RSC Adv.*, 2024, **14**, 38044

Fabrication of $BiVO_4/Ag_2CrO_4$ heterojunction composites modified with graphene oxide for enhanced photoelectrochemical and photocatalytic performance†

Adewunmi Olufemi Oluwole, [a] Tunde L. Yusuf, [b] Shepherd M. Tichapondwa,[a] Michael O. Daramola[a] and Samuel A. Iwarere *[a]

A novel GO/$BiVO_4/Ag_2CrO_4$ heterojunction photocatalyst was prepared by depositing Ag_2CrO_4 on the highly active (040) facet of $BiVO_4$, followed by incorporating graphene oxide (GO) through an *in situ* precipitation method. This synergistic modification of $BiVO_4$ by Ag_2CrO_4 and GO results in excellent photocatalytic performance, with a degradation efficiency of 94.6% coupled with a maximum rate constant of 0.223 min^{-1}, which is 2.40, 2.19 and 0.66 times higher than that of $BiVO_4$, Ag_2CrO_4, and $BiVO_4/Ag_2CrO_4$, respectively, for the degradation of ciprofloxacin (CIP) under visible light irradiation. The degradation efficiency of ciprofloxacin was evaluated using total organic carbon (TOC) analysis. Under investigated conditions, the GO/$BiVO_4/Ag_2CrO_4$ photocatalyst achieved a TOC reduction of 63.4%. The enhanced photocatalytic performance is attributed to the beneficial role of GO in facilitating electron transport for photo-charge carrier migration, leading to strong interfacial coupling between $BiVO_4$ and Ag_2CrO_4, which in turn promotes efficient charge separation and transfer. The physicochemical properties of the fabricated heterojunction photocatalysts were characterized using X-ray diffraction (XRD), field emission-scanning electron microscopy (FE-SEM), transmission electron microscopy (TEM) coupled with energy-dispersive X-ray (EDX) analysis, Brunauer–Emmett–Teller (BET) analysis, Fourier-transform infrared (FTIR) spectroscopy, ultraviolet-visible diffuse reflectance spectroscopy (UV-DRS), and photoluminescence (PL) emission spectroscopy, while the photoelectrochemical properties of the fabricated photocatalyst were investigated through electrochemical impedance spectroscopy (EIS), Mott–Schottky plots, and photocurrent response analysis. The scavenging experiment was conducted to confirm the role of H^+ and $\cdot O_2^-$ in the photocatalytic degradation of ciprofloxacin, which aids in proposing probable degradation mechanism for ciprofloxacin under visible light irradiation. Hence, this study offers an effective strategy for fabricating heterojunction photocatalysts aimed at enhancing the photodegradation of pollutants in wastewater.

Received 4th October 2024
Accepted 15th November 2024

DOI: 10.1039/d4ra07144a

rsc.li/rsc-advances

Introduction

Over the last decades, the pollution of the environment through the discharge of various organic, inorganic and pharmaceutical compounds has forced researchers to develop novel systems for the removal and degradation of such environmental pollutants.[1,2] The increased consumption of pharmaceutical compounds, especially antibiotics for human and livestock disease treatment, can be attributed to the increase in world population.[3–5] The presence of antibiotics in aquatic environments, even at low concentrations, may induce an imbalance in the aquatic ecosystem and human health through the proliferation of bacterial drug resistance.[6–8] CIP is a member of the fluoroquinolone group of antibiotics that shows broad-spectrum antimicrobial activity.[9] Nevertheless, owing to its high structural stability, CIP cannot be effectively metabolized in the human body, and as a result, its residues spread throughout the environment causing serious health problems because of its toxicities and high resistance to degradation as it can accumulate in the living organism within the environment.[10,11] Over the last decades, researchers have utilized many techniques, including absorption, ozonolysis, electrolysis, membrane separation, photocatalysis, and microbial decomposition, for the removal of these pharmaceutical compounds from water.[12–14] Among these techniques, photocatalysis has

[a]*Department of Chemical Engineering, Faculty of Engineering, Built Environment and Information Technology, University of Pretoria, Hatfield, Pretoria 0002, South Africa. E-mail: samuel.iwarere@up.ac.za*

[b]*Department of Chemistry, Faculty of Natural and Agricultural Sciences, University of Pretoria, Hatfield, Pretoria 0002, South Africa*

† Electronic supplementary information (ESI) available. See DOI: https://doi.org/10.1039/d4ra07144a

been proven to be a desirable approach for the degradation of pharmaceutical compounds in wastewater, which can be attributed to its high efficiency, high energy-conservation and low cost.[15,16] It is important to note that the application of frequently used photocatalyst semiconductors, including TiO_2, ZnO, Al_2O_3, SnO_2, WO_3, ZrO_2, CuO, and MoS_2, has limitations such as low adsorption capacity for hydrophobic pollutants and inefficiency in the utilization of abundant visible light under solar irradiation.[11,17–19]

Bismuth-oxide-based semiconductors such as bismuth vanadate ($BiVO_4$) have been widely studied in the field of visible-light photocatalysis as a result of their narrow bandgap (around 2.4 eV), good visible light absorption, stable photo-corrosion resistance, versatile structural and electronic properties and less expensiveness.[12,19,20] Nevertheless, the photocatalytic efficiency of $BiVO_4$ remains unsatisfactory for the degradation of pharmaceutical compounds in water. This is primarily due to its high recombination rate of photo-generated electron–hole pairs, low utilization efficiency of visible light, and weak surface adsorption properties.[21–23] Moreover, despite the narrow band gap of $BiVO_4$, its valence band (VB) and conduction band (CB) potentials are insufficiently positive or negative with its photo-generated electrons and holes lacking redox activity, and this will make the generation of free radicals such as hydroxyl radicals ($\cdot OH$) or superoxide radicals ($\cdot O_2^-$) difficult resulting in low photocatalytic efficiency in the degradation of pharmaceutical compounds.[22,24] Therefore, many methods such as doping with other photocatalyst materials *via* modification have been initiated to improve the photocatalytic efficiency of $BiVO_4$ composites where the synthesis of heterojunction photocatalysts is considered the most convenient and efficient technique to overcome the problems associated with severe photogenerated electron–hole recombination and poor redox capacity of pristine $BiVO_4$. The exploration of silver-based semiconductor materials such as silver chromate (Ag_2CrO_4), a new visible-light-driven photocatalyst, has attracted attention recently. This is due to its high photocatalytic performance as a result of its small band gap at about 1.8 eV with an efficient electronic structure associated with the SPR effects of Ag^0 and strong absorption in the visible-light field.[25,26] However, just like many of the single semiconductors, the photocatalytic efficiency of Ag_2CrO_4 suffers from rapid electron–hole recombination. Additionally, Ag_2CrO_4 is slightly soluble in aqueous solutions. Its self-photo-corrosion and limited solubility, similar to what is observed in other Ag-containing photocatalysts, contribute to a reduction in the photocatalytic stability of Ag_2CrO_4.

Therefore, the hybridization of a single semiconductor with other semiconductors or metal oxides with a suitable band structure has proven to be an effective fabrication strategy to tackle the challenges associated with the separation of photo-induced electron–hole pairs.[27,28] The development of heterojunctions between semiconductors such as $BiVO_4$, SnO_2, Ag_2CrO_4, CuO, ZnO and TiO_2 has proven to be an effective and easy approach to facilitate the photo-generated charge separation efficiency and enhance the photocatalytic activity of these unitary semiconductors.[26,28,29] In spite of the efficiency observed in the design of heterojunction composites *via* the combination of two or three nanostructure semiconductors, their photocatalytic efficiency still experiences some limitation as a result of the marginal absorbance in the visible region. Carbon-based materials such as activated carbon, graphene oxide, reduced graphene oxide and carbon nanotubes are good choices for efficient charge transfer.[30,31] The conjunction of graphene oxide with semiconductors or metal oxides has demonstrated exceptional photocatalytic performance for the degradation of organic pollutants in aqueous matrices.[32,33] This can be attributed to its high conductivity, provision of strong UV and visible-light absorption, and facilitated electron transport, which in turn inhibit charge recombination and thermal and mechanical stability.[34–36] GO can act as a sacrificial electron acceptor in composites such as GO/$BiVO_4$/Ag_2CrO_4. Due to its high electron mobility and the presence of electron-attracting oxygen functional groups, GO can accept and transport photoexcited electrons from Ag_2CrO_4. This minimizes the likelihood of Ag^+ being reduced to Ag^0, stabilizing the photocatalyst. By accepting electrons from Ag_2CrO_4, GO helps maintain effective charge separation, reducing electron–hole recombination. This prolonged lifetime of photogenerated holes enables sustained oxidation of pollutants, enhancing the overall photocatalytic efficiency of the system under visible light. The reduction of Ag^+ to Ag^0 within Ag_2CrO_4 during photocatalysis can degrade the material and reduce its stability. GO, by capturing these electrons, reduces the chance of Ag^+ being converted into metallic Ag, thus minimizing photocorrosion and extending the operational lifetime of the composite.

In this research, a heterostructure composite of GO/$BiVO_4$/Ag_2CrO_4 was synthesized, for the first time, by an *in situ* precipitation method. The electron sinks and plasmonic effects of GO and Ag_2CrO_4 facilitate the separation of photogenerated electrons and holes, thereby enhancing the photocatalytic degradation performance of ciprofloxacin under visible light irradiation. The structural, morphological, and optical properties of the GO/$BiVO_4$/Ag_2CrO_4 nanostructures are reported herein.

Experimental

Materials

Chemicals and reagents including graphite powder (99.9%), sulfuric acid (H_2SO_4, 98%), potassium permanganate ($KMnO_4$, 98.5%), hydrochloric acid (HCl, 35%), hydrogen peroxide (H_2O_2, 30%), nitric acid (HNO_3, 68%), bismuth nitrate pentahydrate ($Bi(NO_3)_3 \cdot 5H_2O$, ≥99%), ammonium metavanadate (NH_4VO_3), *tert*-butyl alcohol (*t*-BuOH), benzoquinone (BQ), ethylenediaminetetraacetate salt (EDTA-2Na), NaOH (≥97%) and ciprofloxacin (>98% purity) were purchased from Sigma-Aldrich, South Africa. All chemicals are of fine analytical grade; hence, they were used without further purification.

Synthesis of $BiVO_4$

The monoclinic $BiVO_4$ nanoparticle was prepared by a hydrothermal method in which stoichiometric amounts of bismuth

nitrate pentahydrate ($Bi(NO_3)_3 \cdot 5H_2O$) and ammonium metavanadate (NH_4VO_3) were dispersed into 30 mL of 4 M HNO_3 aqueous solution under ultrasonic treatment for 30 min, respectively. These two solutions were mixed under magnetic stirring for 1 h at room temperature. Solutions of NaOH and HNO_3 were used to adjust the pH of the mixture to 7 under stirring for further 1 h. The stirred mixture was later transferred into a 100 mL Teflon-lined stainless autoclave and sealed. The autoclave was finally put into an oven and maintained at a temperature of 180 °C for 16 h, after which it was allowed to cool down to room temperature. The as-prepared $BiVO_4$ samples were later centrifuged, washed with deionized water (D.I. H_2O) and ethanol for several times and finally dried at 70 °C overnight.

Preparation of GO

GO was synthesized by improved Hummers' method.[37] A concentrated mixture of H_2SO_4 (184 mL) and HNO_3 (48 mL) was added to 1 g of graphite powder and stirred at room temperature until the powder was fully dispersed. After cooling the mixed solution to around 20 °C in an ice bath, 6 g of potassium permanganate ($KMnO_4$) was slowly added. The obtained mixed solution was heated in a water bath to 85 °C and maintained for 30 min until a bright yellow suspension was obtained. Then 10 mL of hydrogen peroxide (H_2O_2) was slowly added to the mixture and allowed to stir for 30 min. The obtained reactants were collected by centrifugation and washed with 10% of HCl and distilled water until the pH value reached 7.0. The reactant black precipitate was dried at 60 °C overnight to obtain GO.

Preparation of Ag_2CrO_4

For the synthesis of Ag_2CrO_4, 1.5 g of $AgNO_3$ was dissolved in 50 mL D.I. H_2O and allowed to stir for 30 min while 0.7 g of K_2CrO_4 dissolved in 20 mL of D.I. H_2O was added. The mixture was allowed to stir at room temperature for 1 h. Afterward, the mixed solution was poured into a 100 mL Teflon-lined autoclave and treated for 18 h at 180 °C in an oven. The resulting product after cooling of the autoclave to room temperature was obtained by centrifugation and washed with water and ethanol severally. The obtained Ag_2CrO_4 precipitate was later dried in an oven at 60 °C overnight.

Preparation of GO/$BiVO_4$/Ag_2CrO_4 nanocomposites

First, 0.01 g of the prepared graphene oxide nanosheets (GO) were dispersed in 50 mL D.I. H_2O with 5 mL of methanol added to enhance the dispersion process and then ultrasonicated for 1 h in order for the prepared GO to be thoroughly dispersed, followed by the addition of 1.00 g of the synthesized $BiVO_4$ under ultra-sonication treatment. Then, 0.178 g of $AgNO_3$ and 0.201 g of polyvinylpyrrolidone were added to the above solution and allowed to vigorously stir for 1 h; afterward, 0.097 g of K_2CrO_4 dissolved in 20 mL of D.I. water was added in a dropwise manner. The resulting solution was further stirred for additional 2 h. The as-synthesized GO/$BiVO_4$/Ag_2CrO_4 nanocomposites were centrifuged, washed thoroughly with distilled water and ethanol until no precipitate of the nanocomposites was seen in the decanted water, and finally dried at 70 °C overnight. The obtained composites of GO/$BiVO_4$/Ag_2CrO_4 were later calcined at 550 °C for 3 h. This process was also used in the synthesis of $BiVO_4$/Ag_2CrO_4 composites but without the introduction of graphene oxide (GO).

Characterization

The crystalline-phase composition of the fabricated nanocomposites was determined using a PANalytical X'Pert Pro powder X-ray diffractometer with Cu-Kα radiation ($\lambda = 1.789$ Å) in θ–θ configuration. SEM equipped with EDS techniques (JEOL Scanning Microscope JSM-6400) was employed to perform imaging and elemental composition analysis, while the microstructure images of the fabricated nanocomposites were further analysed using a JOEL JEM 2100F, 200 kV transmission electron microscope (TEM). The specific surface area and pore distribution of the nanocomposites were investigated using a Brunauer–Emmett–Teller (BET) Micromeritics Tristar II 3020 Version 3.02 system after degassing overnight at 100 °C prior to analysis. Fourier-transform infrared (FT-IR) spectra of the samples were recorded using a PerkinElmer Spectrum One spectrometer with KBr pellets. The light absorption performance of the nanocomposites was evaluated using a UV-vis spectrophotometer (Agilent Technologies Cary 60 UV-vis, Malaysia) while an Autolab Potentiostat (PGSTAT204, Netherlands) workstation was used for electrochemical impedance spectroscopy (EIS), Mott–Schottky plots and photocurrent response analysis of the synthesized heterostructure composites. A Shimadzu TOC-V analyzer was used to quantitatively assess the extent of ciprofloxacin mineralization before and after the photocatalysis reaction.

Photoelectrochemical experiments

The photoelectrochemical characteristics of the prepared nanocomposite samples were measured using a standard three-electrode cell in the presence of the fabricated anode, a platinum wire and Ag/AgCl (3.0 M KCl) to function as the working, counter and reference electrodes, respectively. The working electrode was prepared by using a fluorine-doped tin oxide (FTO) substrate coupled with a geometric area of 1.5 cm by 1.5 cm coated with 30 mg of the fabricated materials, while 5 wt% PVDF and 100 μL NMP serve as binders.[38] Then 5 mM $[Fe(CN)_6]^{3-}$/$[Fe(CN)_6]^{4-}$ in 0.1 M KCl was prepared for the analysis of the electrochemical impedance spectroscopic analysis with collected data analyzed using the Randles circuit model. The photocurrent density was obtained in 0.1 M Na_2SO_4, with an applied bias potential of 1.5 V relative to the Ag/AgCl reference electrode while the Mott–Schottky measurements were conducted under dark conditions using a 5 mM $[Fe(CN)_6]^{3-}$/$[Fe(CN)_6]^{4-}$ solution in a 0.1 M KCl electrolyte.

Results and discussion

X-ray diffraction of the synthesized samples was investigated to characterize their crystal-phase structure, and the patterns are shown in Fig. 1. The peaks of the prepared $BiVO_4$ corresponded

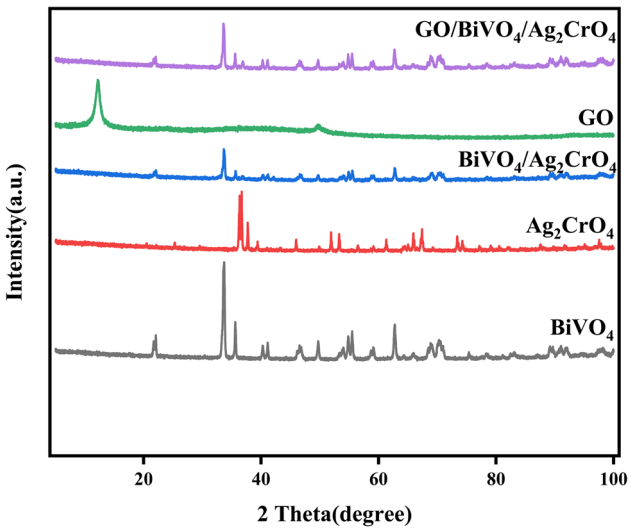

Fig. 1 XRD of the fabricated $BiVO_4$, Ag_2CrO_4, $BiVO_4/Ag_2CrO_4$ and $GO/BiVO_4/Ag_2CrO_4$ heterojunction photocatalysts.

to the characteristic peaks of monoclinic $BiVO_4$ (JCPDS: 14-0688) while the diffraction crystallinity peaks observed for pure Ag_2CrO_4 resulted from its orthorhombic structure (JCPDS no. 26-0952).[39,40] The diffraction peaks observed for $BiVO_4/Ag_2CrO_4$ are linked to $BiVO_4$ and Ag_2CrO_4 with lower amplitudes. However, the diffraction pattern of pure GO shows the characteristic peak due to its interlayer stacks indexed to the (001) and (100) diffraction planes of its oxygen-containing functional group.[41] The characteristic peaks of the fabricated $GO/BiVO_4/Ag_2CrO_4$ heterojunction composites are similar to the binary composites of $BiVO_4/Ag_2CrO_4$, which indicates that compositing GO and Ag_2CrO_4 did not significantly change the crystal morphology of $BiVO_4$ with diffraction peaks of $BiVO_4$ dominant due to its crystallinity.

The crystal size of the fabricated nanocomposites was calculated according to the Scherrer formula S2.†[42] As provided in Table 1, it can be seen that the introduction of Ag_2CrO_4 into $BiVO_4$ caused a significant reduction in the crystallite size of $BiVO_4$ from 44.72 nm to 32.68 nm with a slight improvement in the crystalline size of the $GO/BiVO_4/Ag_2CrO_4$ heterojunction photocatalyst (36.16 nm), suggesting a better photocatalytic activity as it has been proven that photocatalysts with smaller particle sizes tend to exhibit better photocatalytic efficiency.[43]

From Fig. 2a, it can be seen that the surface architecture of the fabricated $BiVO_4$ composites displayed a well-defined flat smooth surface with sharp edges and a decagonal shape from

Table 1 Textural characteristics of the fabricated nanocomposites

Photocatalyst material	Surface area ($m^2\ g^{-1}$)	Pore volume ($cm^3\ g^{-1}$)	Pore diameter (nm)	Crystalline size (nm)
$BiVO_4$	0.605	0.00036	13.80	44.72
Ag_2CrO_4	0.814	0.0014	69.43	30.85
GO	1023.42	0.63	76.91	9.33
$BiVO_4/Ag_2CrO_4$	3.563	0.00074	27.61	32.68
$GO/BiVO_4/Ag_2CrO_4$	17.141	0.00081	37.36	36.16

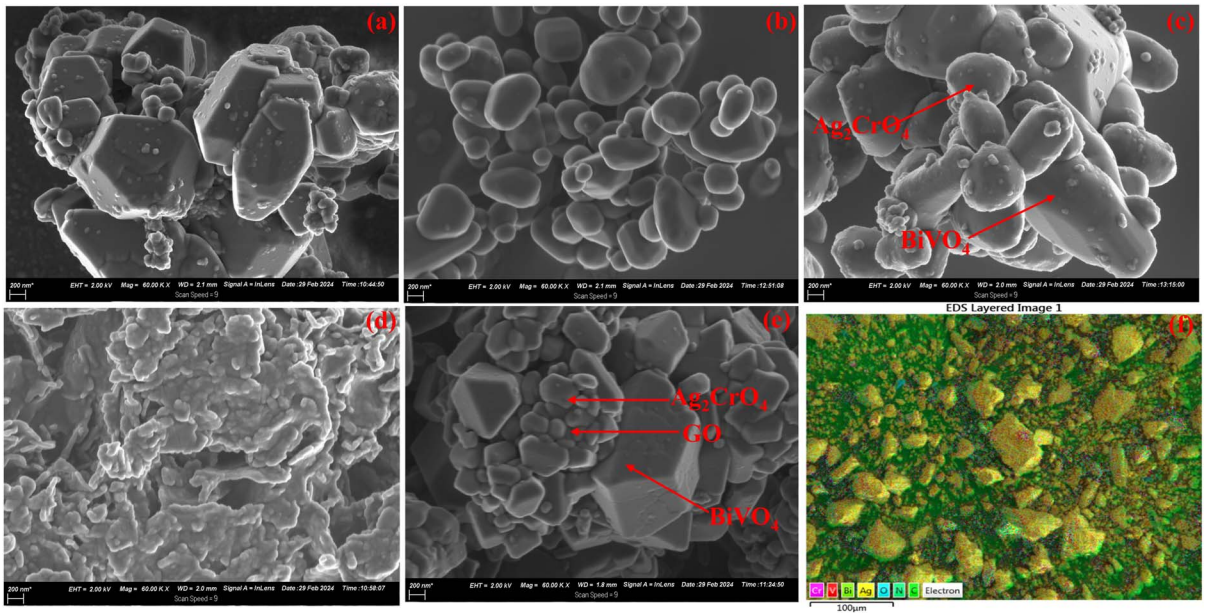

Fig. 2 SEM micrographs of (a) $BiVO_4$, (b) Ag_2CrO_4, (c) $BiVO_4/Ag_2CrO_4$, (d) GO, (e) $GO/BiVO_4/Ag_2CrO_4$, and (f) EDS mapping of $GO/BiVO_4/Ag_2CrO_4$ nanocomposites.

SEM analysis. Two facets are also observed in the morphology, which can be attributed to (040) and (110), while these facets are responsible for the transfer of charge carriers.[44] The prepared Ag_2CrO_4 sample represents a cluster of cube-like nanostructures and particle-like microstructures. The SEM image of binary $BiVO_4/Ag_2CrO_4$ shows a microsphere-type morphology, with the aggregation of the cube-like nanostructures of Ag_2CrO_4 on the surface of $BiVO_4$ as they are seen to maintain their original morphology after the introduction of Ag_2CrO_4 nanoparticles, as it can reduce the charge carrier recombination rates, hence promoting the photocatalytic performance.[45] As shown in Fig. 2e, the addition of GO into the $BiVO_4/Ag_2CrO_4$ nanocomposites increases the space between nanostructures on the microspheres' surface, resulting in an enhanced specific surface area and generation of more active sites.

Energy-dispersive spectrum (EDS) studies were used to reveal the chemical composition of the fabricated $GO/BiVO_4/Ag_2CrO_4$ nanocomposite. Seven elements including C, Bi, O, N, V, Ag, and Cr were found on the surface of the fabricated $GO/BiVO_4/Ag_2CrO_4$ nanocomposite, as shown in the EDS elemental mapping and composition in Fig. 3, proving that the nanocomposite is without impurity, which is consistent with the XRD results.

TEM analysis was used to provide further structural and crystal phase analyses of the fabricated $GO/BiVO_4/Ag_2CrO_4$ nanocomposites. Fig. 4a indicates that the synthesized $BiVO_4$ composites are made up of aggregated decagonal shapes of nanoparticles, which is consistent with the SEM result. The TEM image of the Ag_2CrO_4 composite shows the presence of dark regions in the Ag_2CrO_4 nanoparticles, which can be attributed to the overlapping within the nanoparticles. The Fig. 4c shows the integration of the dark nanoparticle of Ag_2CrO_4 on the surface of the spherical nanosheets of $BiVO_4$, while the particles of Ag_2CrO_4 and the lamellar sheets of GO are spread over the surface of $BiVO_4$ microspheres, as shown in Fig. 4e for the fabricated $GO/BiVO_4/Ag_2CrO_4$ nanocomposite. The close interaction observed in the fabricated $GO/BiVO_4/Ag_2CrO_4$ nanocomposite suggests the formation of heterojunction between GO, $BiVO_4$ and Ag_2CrO_4 which is advantageous for the separation of charge carriers, thereby confirming the successful fabrication of the ternary $GO/BiVO_4/Ag_2CrO_4$ nanocomposites.[46]

The surface functional groups present in the synthesized $BiVO_4$, Ag_2CrO_4, GO, $BiVO_4/Ag_2CrO_4$ and $GO/BiVO_4/Ag_2CrO_4$ samples were investigated by FTIR spectroscopy, and the results are shown in Fig. 5. For $BiVO_4$, the absorption peaks observed at 3436 cm^{-1} are assigned to the bending vibration of residual H_2O molecules adsorbed on the surface of the synthesized $BiVO_4$. This absorbed H_2O molecule can be converted into hydroxyl radicals during the degradation process.[47] The peak at 430 cm^{-1} is characteristic of the bending vibration of Bi–O, while the strong bands at 740 cm^{-1} are attributed to the monoclinic scheelite of $BiVO_4$ due to the asymmetric stretching of the V–O bond. The bands at 1314, 1637, 2345 and 2926 cm^{-1} belong to the bending vibration of the residual NO_3^-, C=O, C–C and C–H bonds.[48] For the FTIR spectra of Ag_2CrO_4, the prominent absorption band at 878 cm^{-1} is ascribed to the Cr–O stretching vibration in CrO_4^{2-} while the absorption peak at 3438 cm^{-1} can be attributed to the O–H group stretching vibration.[49] In the spectra of GO, the characteristic peaks at 1732, 1613, and 1109 cm^{-1} can be ascribed to carboxyl C=O stretching, carboxyl-OH stretching, and alkoxy C–O stretching with the strong absorption band at 3410 cm^{-1} attributed to the OH stretching vibration.[50] The FTIR spectrum of the $BiVO_4/Ag_2CrO_4$ and $GO/BiVO_4/Ag_2CrO_4$ composites represents the overlap spectra of $BiVO_4$, Ag_2CrO_4 and GO, which indicates that the synthetic process is successful.

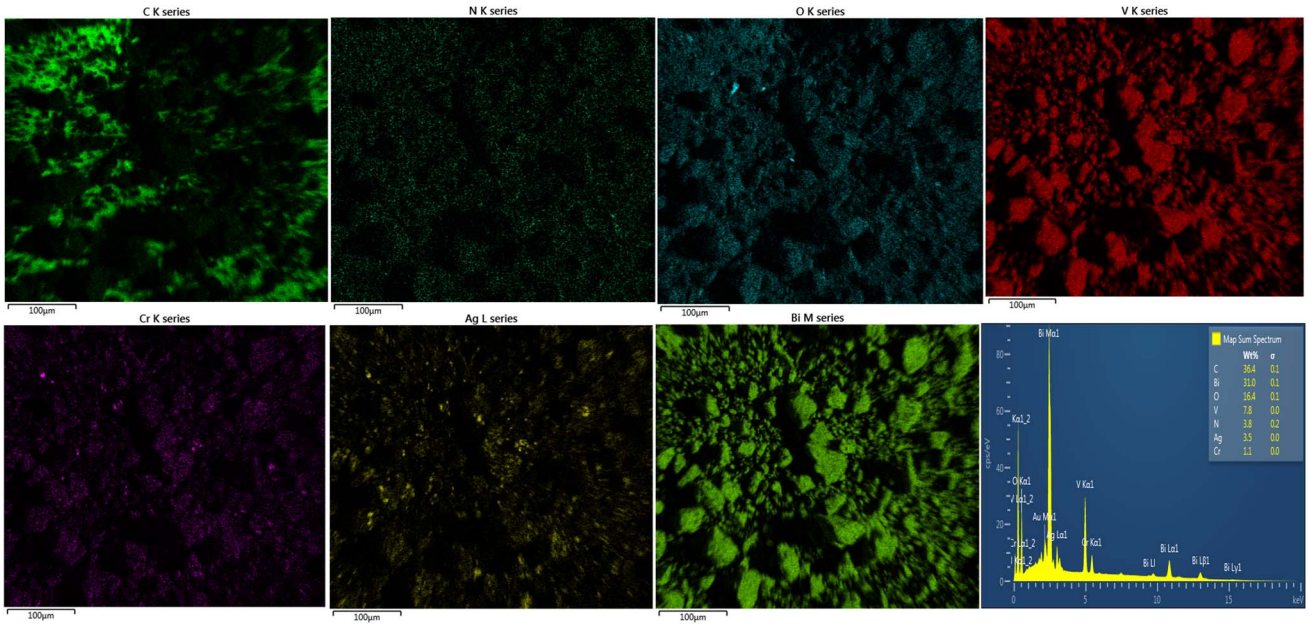

Fig. 3 Elemental mapping and EDS spectra of $GO/BiVO_4/Ag_2CrO_4$ nanocomposites.

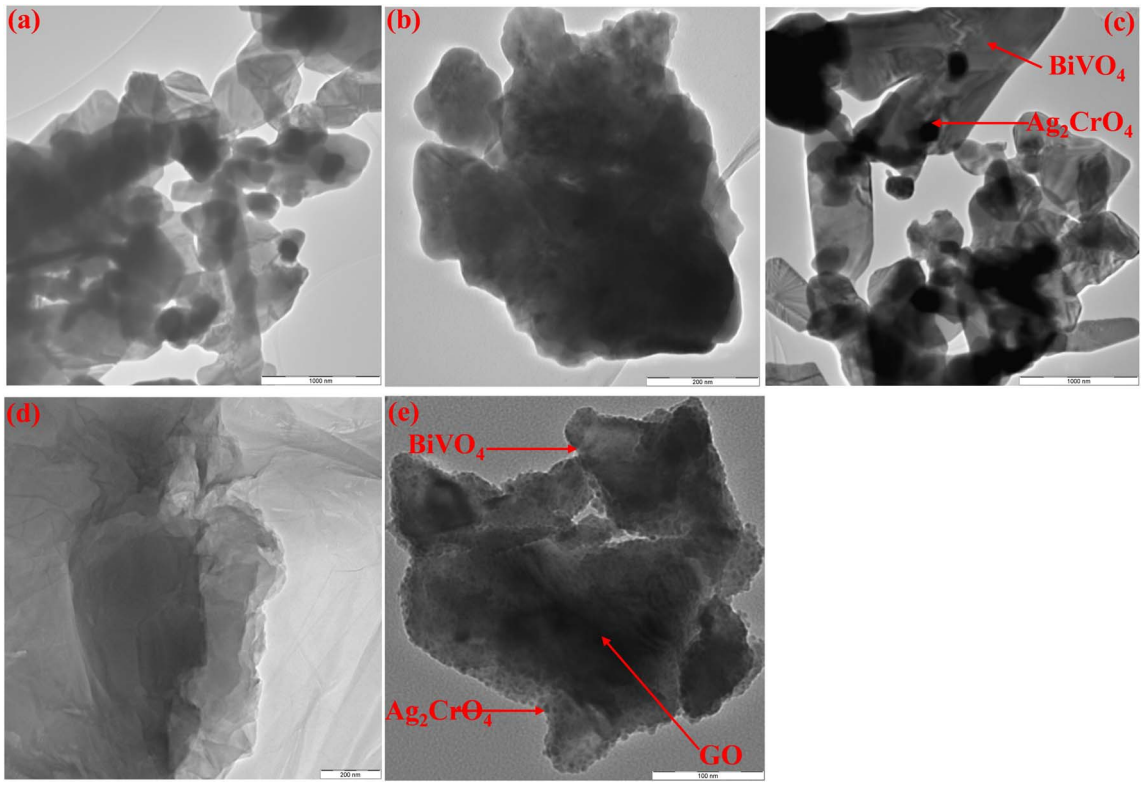

Fig. 4 TEM micrographs of (a) $BiVO_4$, (b) Ag_2CrO_4, (c) $BiVO_4/Ag_2CrO_4$, (d) GO and (e) $GO/BiVO_4/Ag_2CrO_4$ nanocomposites.

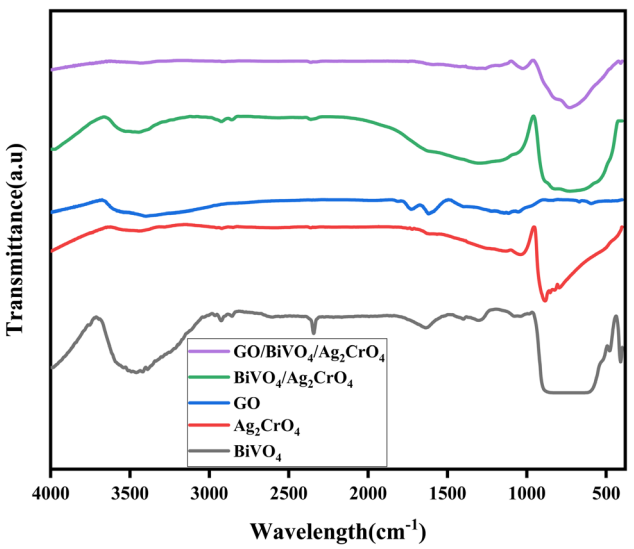

Fig. 5 Fourier transform infrared (FTIR) spectra of the fabricated $BiVO_4$, Ag_2CrO_4, $BiVO_4/Ag_2CrO_4$, GO and $GO/BiVO_4/Ag_2CrO_4$ nanocomposites.

The surface area, pore volume, and pore size distributions of the synthesized materials were analysed using the BET nitrogen adsorption–desorption isotherm. Fig. 6 shows the isotherms of the synthesized nanocomposites to exhibit an H3 hysteresis loop with a type IV isotherm, which designates the occurrence of mesopores in the synthesized materials, which can play a significant role in the degradation of organic pollutants in water.[51]

It was determined from the BET analysis that the surface area of $BiVO_4$, Ag_2CrO_4 and GO is 0.605, 0.814 and 1023.42 $cm^2 g^{-1}$, respectively, whereas the surface area of $BiVO_4/Ag_2CrO_4$ and $GO/BiVO_4/Ag_2CrO_4$ is 3.563 and 17.141 $cm^2 g^{-1}$, which are greater than that of $BiVO_4$ and Ag_2CrO_4. Thus, the $GO/BiVO_4/Ag_2CrO_4$ nanocomposites conserve the surface texture of its components ($BiVO_4$, Ag_2CrO_4 and GO) and the remarkable surface area offers a large number of vigorous sites to adsorb the organic contaminants, which may be advantageous in enhancing its photocatalytic activities. The values of pore volume and pore size distribution are highlighted in Table 1, and the synthesized nanocomposites of $GO/BiVO_4/Ag_2CrO_4$ exhibit an improved pore volume and pore size when compared to the other materials due to the presence of GO.

Electrochemistry analysis

The photocatalytic performance of photocatalyst materials largely depends on the absorption of visible light; therefore, it is important to investigate the absorption ability of the synthesized materials using UV-vis diffuse reflectance spectrum (DRS), and the results are shown in Fig. 7. All the synthesized materials absorb photons in the visible region at 535 nm, 751 nm, 722 and 734 nm for $BiVO_4$, Ag_2CrO_4, $BiVO_4/Ag_2CrO_4$ and $GO/BiVO_4/Ag_2CrO_4$ respectively. The shift in the absorption edge of $GO/BiVO_4/Ag_2CrO_4$ towards the near-infrared region with increased absorption can be attributed to the interaction of $BiVO_4$ with

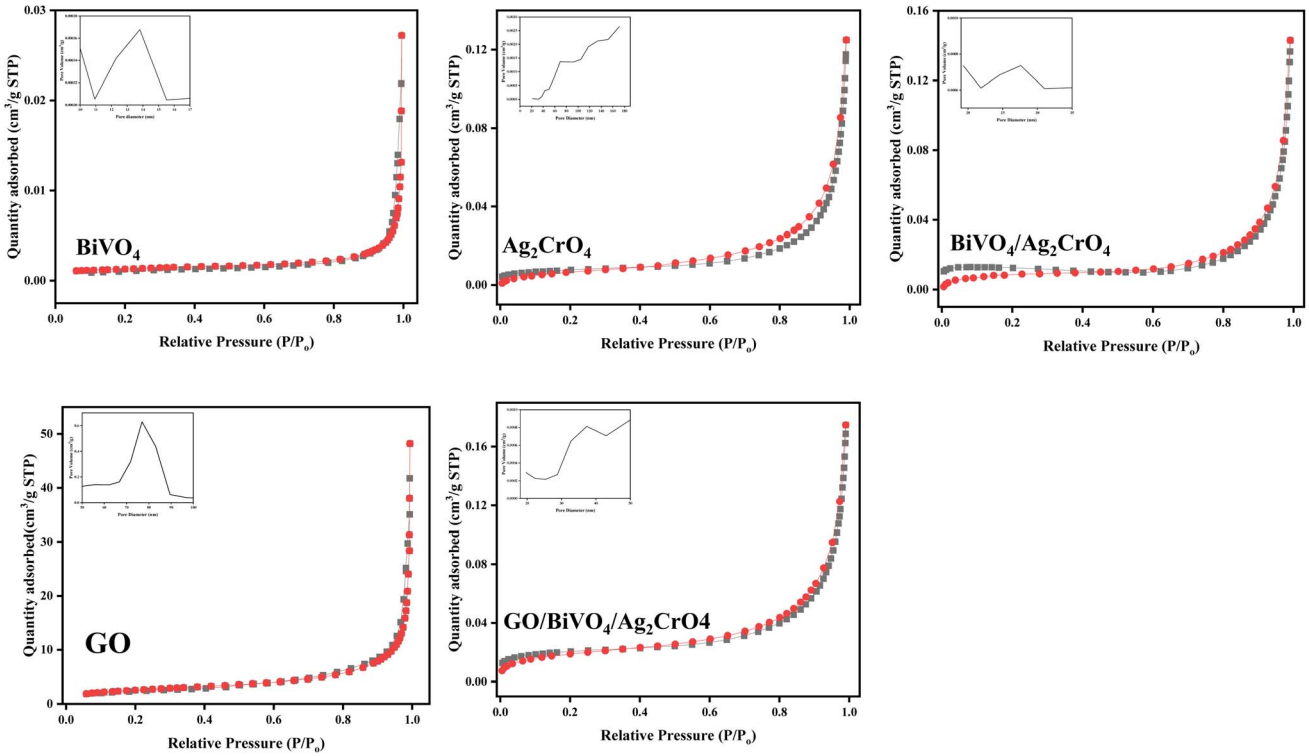

Fig. 6 Nitrogen sorption isotherms and the corresponding pore volume and diameter distribution of the fabricated nanocomposites.

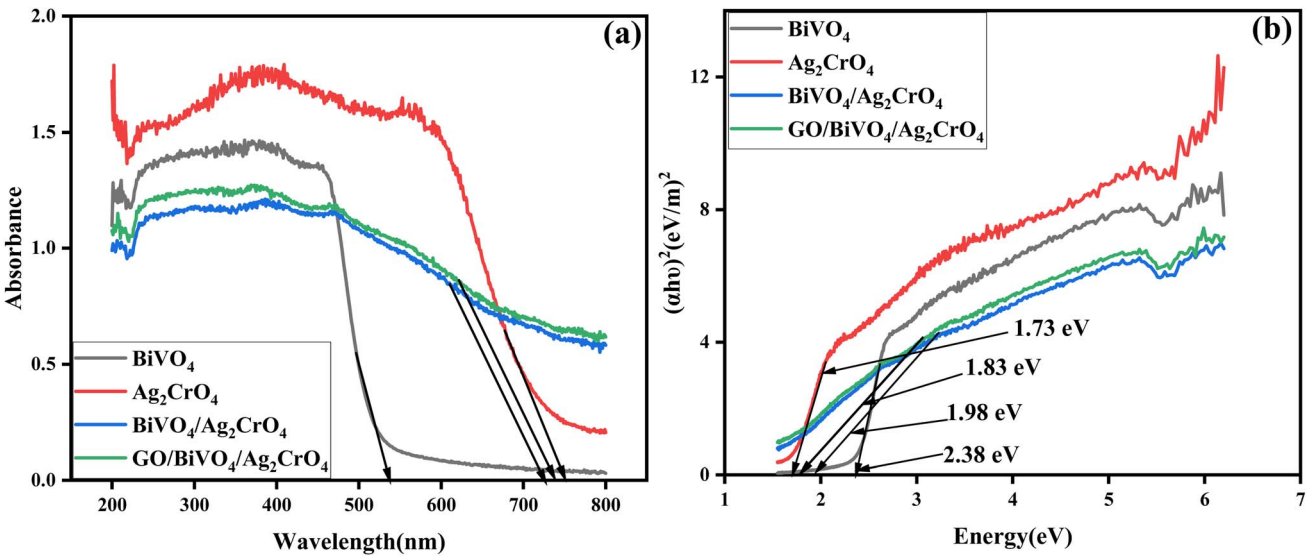

Fig. 7 UV-vis DRS spectra of the fabricated nanocomposites with their corresponding Tauc plots.

Ag_2CrO_4 and with the inclusion of GO *via* compositing, where GO functions as a matrix in enhancing light adsorption capacity in the visible light region with a redshift. The data obtained from the UV-DRS analyses were used to investigate the band gap energy of the synthesized nanocomposites using the Tauc equation, as given in eqn (1):

$$\alpha h\nu = A(\nu h - E_g)^{n/2} \quad (1)$$

where α, h, A, E_g and ν represent the absorption coefficient, Planck's constant, constant, band gap energy, and incident light frequency and 'n' is a constant that depends solely on the optical transition characteristics of the semiconductors under consideration.[52] As shown in the figure, the energy bandgaps of $BiVO_4$, Ag_2CrO_4, $BiVO_4/Ag_2CrO_4$ and $GO/BiVO_4/Ag_2CrO_4$ were calculated to be 2.38, 1.73, 1.98 and 1.83 eV respectively. The calculated results inferred that the fabricated graphene-bridged

$BiVO_4/Ag_2CrO_4$ nanocomposites could improve the optical absorption due to co-catalytic interactions between $BiVO_4$/Ag_2CrO_4 composites and GO, which is beneficial for the generation of more electron–hole pairs, resulting in greater photocatalytic efficiencies towards the degradation of organic pollutants in aqueous matrices.

Photoluminescence emission spectra analysis has proven to be one of the effective approaches in understanding the separation capacity of the photoinduced carriers of nanocomposite materials due to the direct result of recombination of the free carriers.[53] Therefore, creating a correlation between the intensity of PL and the photocatalytic activities of the synthesized material as lower recombination of the photogenerated charge carrier originating from a lower PL intensity will result in enhanced photocatalytic activities and *vice versa*. The PL spectra of the synthesized $BiVO_4$ catalyst show a strong emission peak at about 562 nm, as presented in Fig. 8a corresponding to the recombination of the hole formed from the hybrid orbitals of Bi 6s and O 2p, and the electron generated from the V 3d orbital.[54] This suggests that $BiVO_4$ possesses a lower separation efficiency of a photo-induced electron–hole, hence less photocatalytic performance. The fluorescence intensity of the nanocomposites of the $GO/BiVO_4/Ag_2CrO_4$ sample was significantly weaker than that of the $BiVO_4$, Ag_2CrO_4 and $BiVO_4/Ag_2CrO_4$ catalysts, which shows the recombination restraint of the electron–hole pairs. The obtained result shows that the reduction in the recombination of the photogenerated charge carrier of the fabricated $GO/BiVO_4/Ag_2CrO_4$ nanocomposites will prove useful during the photocatalytic degradation of organic pollutants in aqueous matrices.

The separation and transfer of electron–hole pairs of the fabricated nanocomposites were analyzed by electrochemical impedance spectroscopy (EIS). The radius of the arc in the Nyquist plot measurements provides information on the charge transfer process with the diameter of the arc, which is characteristic of the charge transfer resistance, where a smaller arc radius indicates higher efficiency in charge transfer.[55] The findings for the fabricated nanocomposites are displayed in Fig. 8b, with the arc radius of $GO/BiVO_4/Ag_2CrO_4$ is smaller than that of pure $BiVO_4$, Ag_2CrO_4 and $BiVO_4/Ag_2CrO_4$, indicating a faster separation and transfer of photogenerated carrier's nanocomposites. This implied that the fabricated $GO/BiVO_4/Ag_2CrO_4$ nanocomposite possessed a greater charge separation efficiency coupled with the decrease in their band gap energy, hence better photocatalytic activity during visible light irradiation.

The transient photocurrent behaviour of the fabricated materials was investigated at 10 second intervals during ON–OFF cycles of xenon lamp irradiation by chronoamperometry with an applied potential of 1.5 V (see Fig. 9). These measurements allowed us to assess the transfer of photoinduced carriers and evaluate the photocatalytic performance of both pristine materials and heterostructures. Specifically, pristine $BiVO_4$ and Ag_2CrO_4 exhibited maximum photocurrent responses of 0.037 and 0.051 mA cm^{-2}, respectively.

However, the fabricated heterostructures demonstrated significantly higher responses. Notably, the combination of $BiVO_4$ and Ag_2CrO_4 enhanced carrier separation and facilitated charge transfer on the catalyst surface. In particular, the $BiVO_4/Ag_2CrO_4$ heterostructure achieved a much higher response, with a recorded maximum photocurrent of 0.070 mA cm^{-2}. However, upon the introduction of GO, the ternary composite $GO/BiVO_4/Ag_2CrO_4$ exhibited a photocurrent maxima of 0.089 mA cm^{-2} which is indicative that the fabricated $GO/BiVO_4/Ag_2CrO_4$ nanocomposite possesses a higher carrier separation efficiency.

Photocatalytic experiments

The photocatalytic activity of the fabricated nanocomposites was tested for the degradation of ciprofloxacin in synthetic water under visible light irradiation (200 W fluorescent lamps). This was done by dispensing 50 mg of each batch of the

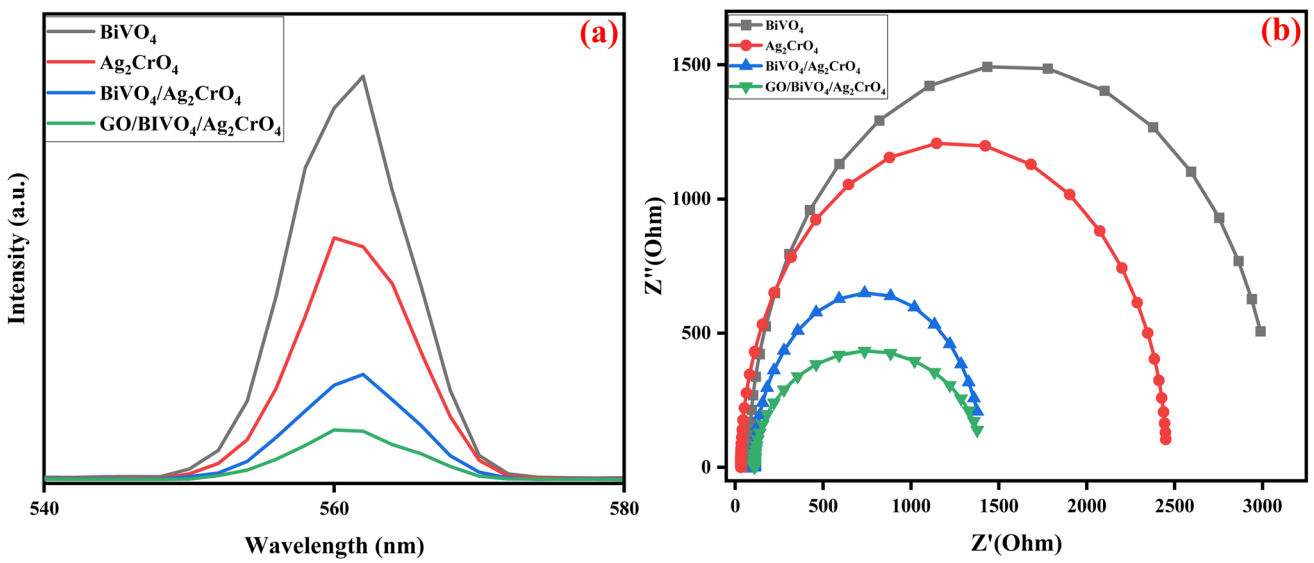

Fig. 8 (a) PL spectra and (b) EIS Nyquist plots of the fabricated nanocomposites.

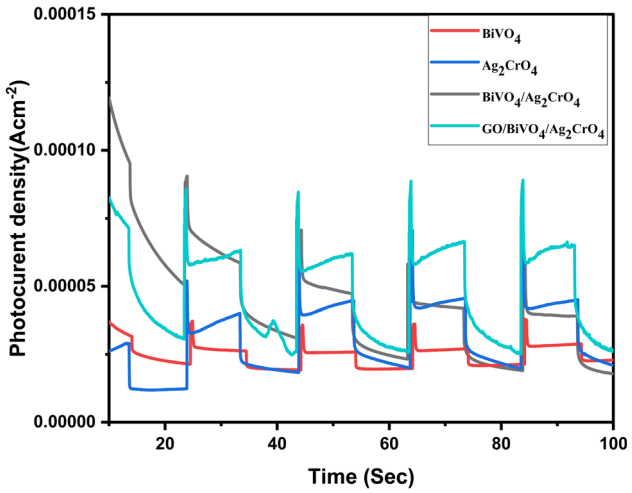

Fig. 9 Photocurrent response plots of $BiVO_4$, Ag_2CrO_4, $BiVO_4/Ag_2CrO_4$, and $GO/BiVO_4/Ag_2CrO_4$ nanocomposites.

composites in 100 mL of 10 mg L^{-1} of ciprofloxacin solution, while the suspension was stirred in the darkness for 30 min to achieve the adsorption–desorption equilibrium between the ciprofloxacin solution and the photocatalyst. At every 20 min interval, 4 mL aliquot samples of the suspension was collected, centrifuged and filtered through a 0.45 μm Millipore filter before analysis using a UV-vis spectrophotometer (Biochrom, Cambridge, UK) to estimate the change in ciprofloxacin concentration at a wavelength of 274 nm. The calculation of the photodegradation percentage was determined using the following equation:

$$\text{Removal efficiency} = \frac{C_0 - C}{C_0} \times 100\% \quad (2)$$

where C_0 stands for the initial concentration of the ciprofloxacin solution at time (t_0) (initial time) before treatment, while C is the concentration value at a final time after treatment.

Adsorption studies for the fabricated composites were carried out under the same condition. The adsorption capacity of the fabricated nanocomposites as presented in S4† shows that $BiVO_4$, Ag_2CrO_4, GO, $BiVO_4/Ag_2CrO_4$ and $GO/BiVO_4/Ag_2CrO_4$ were able to adsorb 20.40, 23.04, 32.43, 40.13 and 45.40% of ciprofloxacin. The absorption ability of the synthesized nanocomposites can be associated with the specific surface area, as shown in Table 1.

The C/C_0 value of the degradation efficiency of the fabricated photocatalyst is displayed in Fig. 10a with the degradation rate provided in Table 2. It can be seen that $BiVO_4$, Ag_2CrO_4, $BiVO_4/Ag_2CrO_4$ mixture and $GO/BiVO_4/Ag_2CrO_4$ achieved 48.64, 55.87, 72.44, 59.03 and 94.56% for the degradation of ciprofloxacin after 120 min of irradiation under visible light. The enhancement in the photodegradation efficiency of $GO/BiVO_4/Ag_2CrO_4$ can be attributed to the incorporation of GO into the fabricated $BiVO_4/Ag_2CrO_4$ composites. This is due to the interaction of the GO sheet with the fabricated $BiVO_4/Ag_2CrO_4$ *via* physical adsorption, increased surface area and electrostatic transfer, resulting in a reduction of the photogenerated electron–hole pair recombination coupled with the electron donation-mediation of surface plasmon resonance (SPR) supplied with the presence of Ag_2CrO_4, hence the improved photocatalytic

Table 2 Kinetic constants (k) for each photocatalyst using a pseudo-first-order model

Photocatalyst material	Degradation (%)	Rate constant k (min^{-1})	Coefficient R^2
Photolysis	13.07	0.03953	0.95143
$BiVO_4$	48.64	0.06572	0.94804
Ag_2CrO_4	55.87	0.06981	0.92836
$BiVO_4/Ag_2CrO_4$	72.44	0.13385	0.95564
Mixture	59.03	0.09959	0.96743
$GO/BiVO_4/Ag_2CrO_4$	94.56	0.22253	0.94652

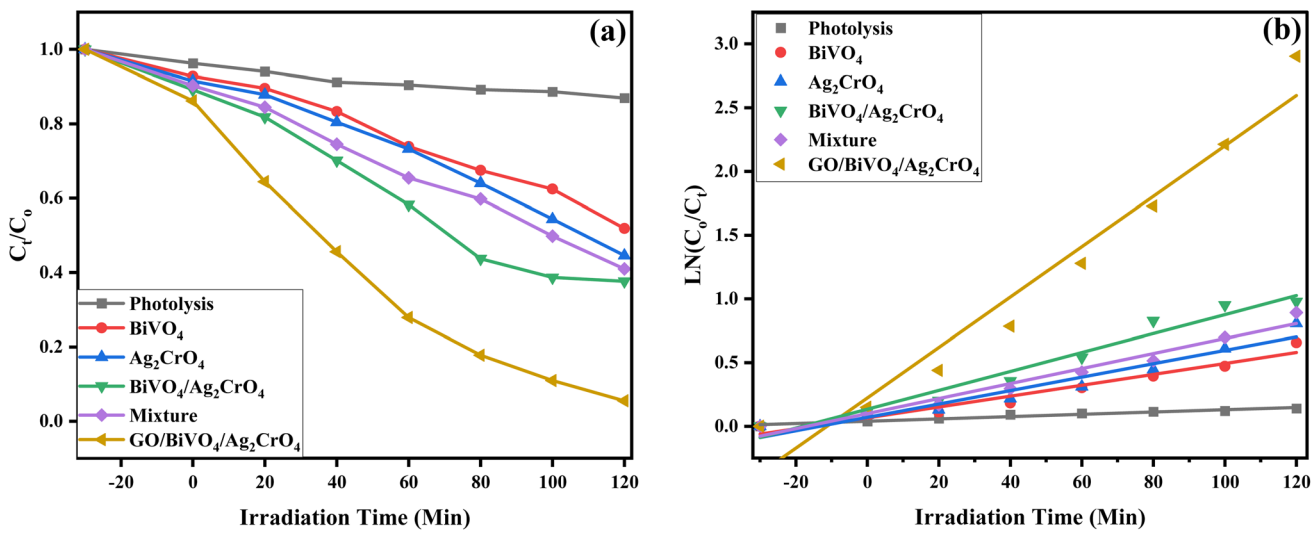

Fig. 10 (a) Degradation plot of ciprofloxacin using the fabricated nanocomposites and (b) their corresponding kinetic plot.

efficiency of $GO/BiVO_4/Ag_2CrO_4$ for the degradation of ciprofloxacin. This is in agreement with the analysis result obtained from UV-DSR, PL, EIS, and BET.

The kinetics of the photocatalytic process was analyzed using the pseudo-first-order kinetic *via* the Langmuir–Hinshelwood model equation as follows:

$$(-\ln(C/C_0) = kt) \quad (3)$$

where C_0 and C stand for the initial and final concentrations of the ciprofloxacin solution at time t, while k represents the reaction rate constant respectively.

Fig. 10b shows that the rate constant of $GO/BiVO_4/Ag_2CrO_4$ was 0.22253 min^{-1}, which was 2.40, 2.19 and 0.66 times higher than that of $BiVO_4$, Ag_2CrO_4, and $BiVO_4/Ag_2CrO_4$ respectively while all the values of the coefficient R^2 were greater than 0.93 (R^2 > 0.93). The result proves that the improvement in the photocatalytic performance is a result of the loading of GO into the composites of $BiVO_4/Ag_2CrO_4$. Furthermore, the degradation efficiency of ciprofloxacin was evaluated using total organic carbon (TOC) analysis. Under optimal conditions, the $GO/BiVO_4/Ag_2CrO_4$ photocatalyst achieved a TOC reduction of 63.4% (Fig. S6†). The degradation of ciprofloxacin by the fabricated novel heterojunction $GO/BiVO_4/Ag_2CrO_4$ photocatalyst was compared with previously reported studies on ciprofloxacin degradation with other photocatalysts, as provided in Table S2.† It can be seen that the $GO/BiVO_4/Ag_2CrO_4$ photocatalyst fabricated in this study displayed better degradation efficiency at a shorter time when compared with other photocatalysts used in ciprofloxacin degradation.

Effect of catalyst dosage

Catalyst dosage was carried out in order to understand the concentration effect that $GO/BiVO_4/Ag_2CrO_4$ will have on the degradation of ciprofloxacin where different weight ratios of $GO/BiVO_4/Ag_2CrO_4$ were used, and their photodegradation performance was evaluated under visible light irradiation. Fig. 11a displays ciprofloxacin photodegradation at 30, 50, 70, and 100 mg weight to achieve 73.24, 94.51, 98.06 and 86.83%, respectively. It can be seen from the result that the optimum loading of the nanocomposites is 70 mg for efficient photodegradation of ciprofloxacin, which can be attributed to the increase in vacant active sites, while the decrease in the photocatalytic degradation of ciprofloxacin at 100 mg can be due to the light reflected by the catalyst particle, thereby preventing the entry of photons into the solution.[56]

Effect of pH

Additionally, investigating the pH level of the reaction medium is one of the major parameters that affect the photocatalytic degradation efficiency of pharmaceutical compounds by influencing the chemical state and surface charge of the fabricated $GO/BiVO_4/Ag_2CrO_4$ nanocomposites, resulting in electrostatic interaction between them.[57] The point of zero charge (pH_{zpc}) of the fabricated $GO/BiVO_4/Ag_2CrO_4$ nanocomposites was analyzed to predict its interaction with the ciprofloxacin pollutant during the degradation process. The pH_{zpc} of the fabricated photocatalyst was evaluated by using the pH drift method described in S4 in the ESI.†[58] As shown in Fig. S4,† the pH_{zpc} of the $GO/BiVO_4/Ag_2CrO_4$ photocatalyst was calculated to be 6.08. Therefore, an experiment on the photodegradation of ciprofloxacin was carried out at different pH values of 2, 4, 6, 8 and 10 (Fig. 11b) with the percentage degradation of ciprofloxacin achieved at 30.34, 64.84, 96.51, 81.04 and 75.03% for pH 2, 4, 6, 8 and 10 respectively. The photocatalytic degradation of ciprofloxacin using the fabricated $GO/BiVO_4/Ag_2CrO_4$ nanocomposites increases from pH 2 to 6 and then decreases. The least degradation of ciprofloxacin by the nanocomposites was observed at pH 2, which can be attributed to catalytic corrosion and electrostatic repulsion between the surface of $GO/BiVO_4/Ag_2CrO_4$ and ciprofloxacin in the acidic medium.[59] A higher degradation of ciprofloxacin (96.51%) was observed at pH 6,

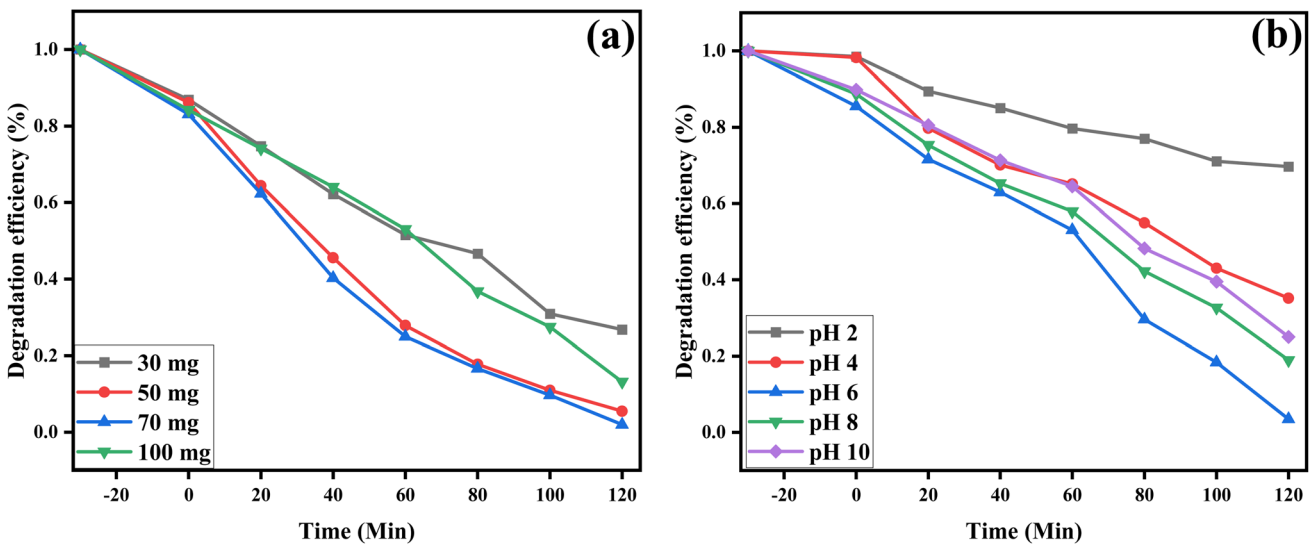

Fig. 11 (a) Effect of dosage plot and (b) pH using the $GO/BiVO_4/Ag_2CrO_4$ nanocomposite.

which indicates that the photocatalytic system is close to the pHpzc of the fabricated GO/$BiVO_4$/Ag_2CrO_4 nanocomposites with the zwitterionic of ciprofloxacin at pK_a1 6.16 and pK_a2 8.23 leading to the minimum electrostatic repulsion between the nanocomposites and ciprofloxacin compounds.[60]

Stability study

The stability of the fabricated nanocomposites for ciprofloxacin degradation was further investigated through four (4) cycling experiments. Four continuous degradation experiments were conducted to degrade ciprofloxacin without changing the nanocomposites. The experiment followed the same procedure of each measurement except for changing the ciprofloxacin solution for each run while the GO/$BiVO_4$/Ag_2CrO_4 nanocomposite was re-collected by centrifugation, rinsed with D.I. H_2O and dried for next cycle run. It can be seen from Fig. 12a that there is only a slight drop in the degradation performance of the nanocomposite after four cycles, which can be due to the loss of the catalyst during each round of catalyst collection.[61] Overall, the obtained result indicated that the fabricated GO/$BiVO_4$/Ag_2CrO_4 is stable, and it can be reusable in photocatalytic processes for the degradation of pharmaceutical compounds in aqueous matrices.

The XRD patterns of both fabricated GO/$BiVO_4$/Ag_2CrO_4 and recycled GO/$BiVO_4$/Ag_2CrO_4 nanocomposites are displayed in Fig. 12b, and it can be seen that a negligible variation in peak intensity between the fresh and recycled nanocomposites was observed, which confirms that the fabricated heterojunction nanocomposites possess a remarkable photostability during the photodegradation processes.[62]

Effect of radical scavenger experiments

Scavenger analyses were performed to determine the most reactive oxidation species in the degradation of ciprofloxacin under visible irradiation and also to provide addition information for the degradation mechanism. This was performed through the addition of 5 mM of ethylenediaminetetraacetate salt (EDTA-2Na for h^+ radicals), *t*-butanol (*t*-BuOH for $OH^{\cdot}$ radicals) and *p*-benzoquinone (*p*-BQE for $\cdot O_2$ radicals).

The results revealed a significant difference in the degradation of ciprofloxacin. Specifically, the use of a ·OH radical scavenger led to a decrease in photodegradation efficiency from 94.56% to 69.80%, while the $\cdot O_2^-$ scavenger and hole scavenger caused a further reduction in the photodegradation of ciprofloxacin noted as 57.21 and 21.00%, respectively, as depicted in Fig. 13. The finding from the scavenging experiment shows that ·OH, $\cdot O_2^-$ and h^+ are the reactive species in the degradation of ciprofloxacin with H^+ and $\cdot O_2^-$ playing a major role in the degradation process when compared to OH radicals.

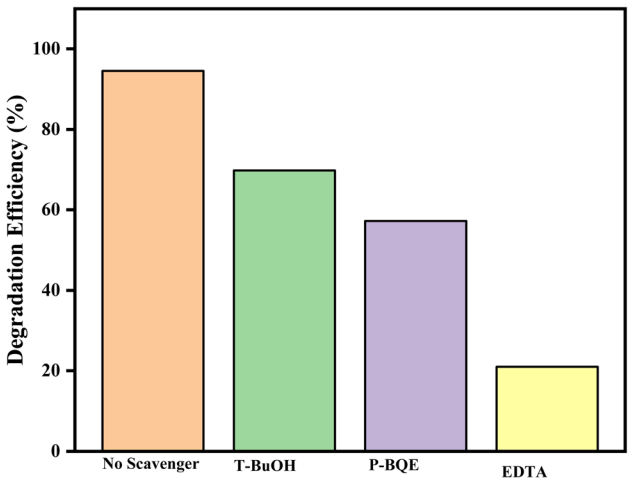

Fig. 13 Detection of reactive species with GO/$BiVO_4$/Ag_2CrO_4 composites during the ciprofloxacin degradation process.

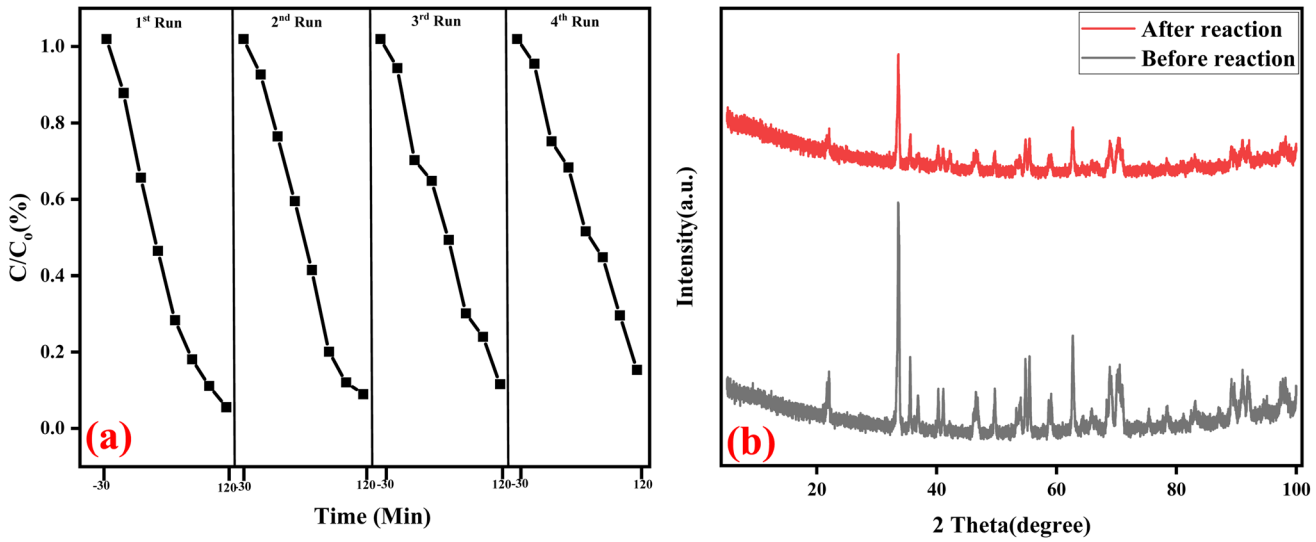

Fig. 12 (a) Successive test run for the degradation of ciprofloxacin and (b) XRD patterns before and after reusing the GO/$BiVO_4$/Ag_2CrO_4 nanocomposites.

Photocatalytic degradation mechanisms

The probable photocatalytic mechanism for the degradation of ciprofloxacin using the fabricated heterojunction GO/$BiVO_4$/Ag_2CrO_4 nanocomposite under visible-light irradiation is schematically illustrated, using the energy band gap results obtained from the UV-DSR analysis of $BiVO_4$ and Ag_2CrO_4 composites (Fig. 7), and their corresponding VB and CB potentials were calculated using Butler and Ginley's equation[63,64] as follows:

$$E_{VB} = X - E^e + 0.5E_g \quad (4)$$

$$E_{CB} = E_{VB} - E_g \quad (5)$$

where E_{VB} and E_{CB} indicate the valence band and conduction band potentials of the composites and X indicates the Mulliken electronegativity of the composites ($BiVO_4$ = 6.04 eV, Ag_2CrO_4 = 5.86 eV), while E^e denotes the energy of free electrons on the hydrogen scale at around 4.5 eV.[23,65] Thereafter, the VB and CB potentials of $BiVO_4$ were calculated to be 2.73 and 0.35 eV, and the VB and CB potentials of Ag_2CrO_4 were calculated to be 2.23 and 0.50 eV, respectively.

Additionally, the Mott–Schottky (M–S) plots shown in Fig. 14 were employed to examine the electronic properties of $BiVO_4$ and Ag_2CrO_4 electrodes. These plots allow for the determination of the flat band potential (E_{fb}) and majority carrier density for each material. The M–S plot for $BiVO_4$ and Ag_2CrO_4 exhibited a positive slope, indicating an n-type semiconducting behaviour. The E_{fb} values derived from the x-axis intercept were 0.54 V and 0.32 V *vs.* the Ag/AgCl reference electrode for Ag_2CrO_4 and $BiVO_4$, respectively. In order to convert these values to the standard hydrogen electrode (NHE) reference scale, the Nernst equation was applied: $E_{NHE} = E_{Ag/AgCl} + 0.197$ (pH). This calculation resulted in E_{fb} values of +0.74 V and 0.52 V *vs.* NHE for Ag_2CrO_4 and $BiVO_4$, respectively. It is also important to consider the typical positioning of the flat band potential relative to the band edges in semiconductors. In n-type materials, the E_{fb} value is generally located at about 0.1–0.3 V above the conduction band (CB) potential. Consequently, the E_{CB} values for $BiVO_4$ and Ag_2CrO_4 were determined to be 0.38 V and 0.51 V *vs.* NHE, respectively. These findings collectively clarify the band energy structures of $BiVO_4$ and Ag_2CrO_4.

Therefore, on the basis of these results, the photocatalytic mechanism of the fabricated GO/$BiVO_4$/Ag_2CrO_4 heterostructure composites is proposed in Fig. 15. The low energy bandgap of the heterostructure GO/$BiVO_4$/Ag_2CrO_4 composites, as investigated using UV-DSR, was helpful in their excitation under visible light irradiation, resulting in reduced electron–hole recombination rates. The valence band and conduction band of the prepared $BiVO_4$ and Ag_2CrO_4 are attached by GO due to their strong interfacial electrostatic interaction.

As shown in Fig. 15, under visible light irradiation, the electron (e^-) on the valence band (VB) of $BiVO_4$ migrated to the valence band (VB) of Ag_2CrO_4, while the holes (h^+) on the VB of $BiVO_4$ are rapidly migrated to the VB of Ag_2CrO_4 under the driving force of the internal electric field and strong interfacial electrostatic interaction provided by GO to achieve the rapid separation of photogenerated charge carriers. The CB potential of $BiVO_4$ and Ag_2CrO_4 is more positive than the standard redox potential of $O_2/\cdot O_2^-$ (−0.33 eV *vs.* NHE); in this instance, it is clear that the photogenerated electrons of $BiVO_4$ and Ag_2CrO_4 in the CB lack sufficient potential to take part in the oxidation process. However, from the scavenger study, $O_2^{\cdot -}$ was mostly responsible for the degradation of CIP where the incorporated GO can serve as an electron acceptor, storing photoexcited electrons generated by the semiconductor components (like $BiVO_4$ or Ag_2CrO_4) in the composite. These stored electrons can be subsequently transferred to molecular oxygen adsorbed on the GO surface, generating superoxide radicals ($O_2^{\cdot -}$). By accepting electrons, GO prevents electron–hole recombination within the photocatalyst system. This leads to a higher number of available electrons that can transfer to oxygen, thereby indirectly boosting superoxide generation. The scavenger results can be justified by elucidating the function of GO in the

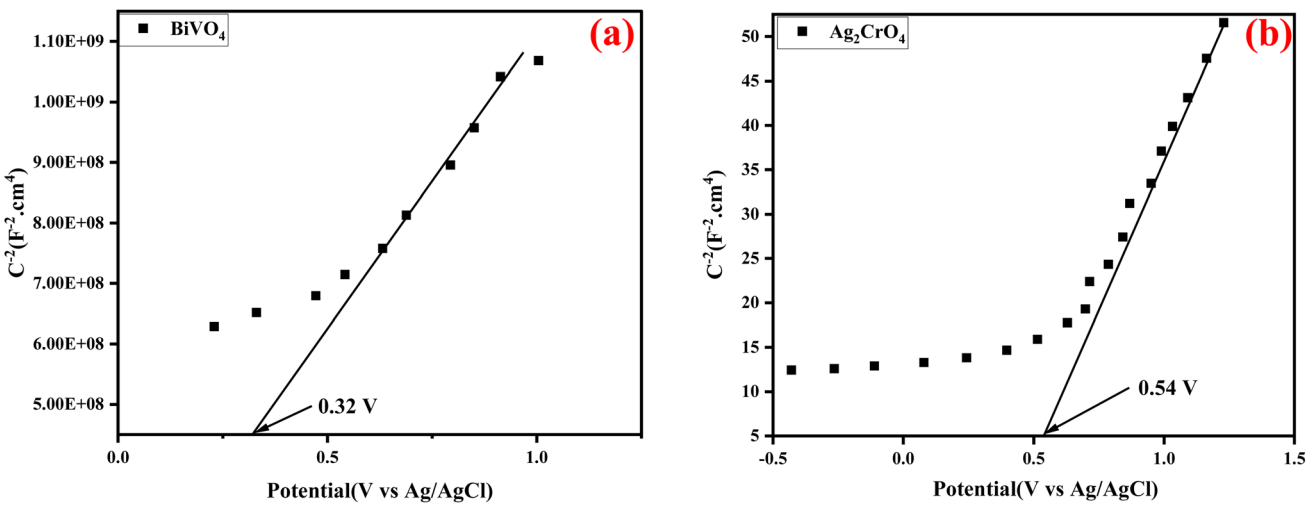

Fig. 14 Mott–Schottky plots of (a) $BiVO_4$ and (b) Ag_2CrO_4.

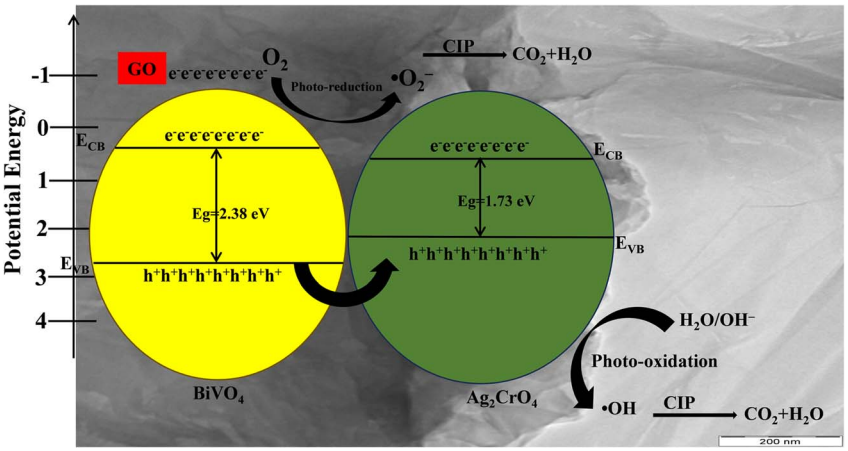

Fig. 15 Possible mechanism for ciprofloxacin photodegradation by the GO/$BiVO_4$/Ag_2CrO_4 photocatalyst.

reduction process, as reported in a previous study[66] and explained as follows:

$$GO + h\nu \rightarrow GO^* \quad (6)$$

$$^3O_2 + GO^* \rightarrow {}^1O_2 \quad (7)$$

$$^1O_2 + GO^* \rightarrow \cdot O_2^- + GO^+ \quad (8)$$

Therefore, GO as an electron mediator increases the contribution of $\cdot O_2^-$ in the photocatalytic activity of the GO/$BiVO_4$/Ag_2CrO_4 photocatalyst. The VB potential of Ag_2CrO_4 is more positive than the standard redox potential of $H_2O/\cdot OH$ (+1.99 eV *vs.* NHE), resulting in the oxidation of H_2O by h^+ to produce $\cdot OH$. It should be noted that the VB potential of $BiVO_4$ is 2.73 eV, which is higher than the standard redox potential of $OH^-/\cdot OH$ (2.4 eV *vs.* NHE) resulting in the oxidation of adsorbed H_2O molecules by the photogenerated h^+ in the VB to produce $\cdot OH$. The proposed mechanism is consistent with the observation made from the scavenging experiment, as shown in Fig. 13, which shows that h^+ and $\cdot O_2^-$ plays a significant role in the degradation of ciprofloxacin when compared to OH radicals when using the fabricated GO/$BiVO_4$/Ag_2CrO_4 heterostructure composites.

Conclusion

In summary, a novel heterojunction visible-light-driven GO/$BiVO_4$/Ag_2CrO_4 photocatalyst has been successfully synthesized *via* an *in situ* precipitation technique and innovatively applied as a highly efficient system in the degradation of ciprofloxacin in simulated water. This excellent multifunctional photocatalytic performance of the fabricated GO/$BiVO_4$/Ag_2CrO_4 photocatalyst may be attributed to the development of a nanohybrid junction between $BiVO_4$ and Ag_2CrO_4 facilitated by the addition of GO in order to promote efficient charge transfer at their interface with improved separation of the photogenerated electrons and holes. The fabricated GO heterojunction photocatalyst also displayed remarkable stability compared to $BiVO_4$ and Ag_2CrO_4, which may be due to the formation of nanohybrids. Based on the active species scavenging experiments and calculated energy band positions, the mechanism of the enhanced photocatalytic activity of the GO/$BiVO_4$/Ag_2CrO_4 photocatalyst was discussed. In general, the $BiVO_4$ hybridized with Ag_2CrO_4 and GO could be used for solving the problems associated with low photocatalytic performance, which will provide a promising way for environmental remediation.

Data availability

The data supporting the findings of this research study are available from the corresponding author upon reasonable request. Additionally, ESI data† and materials have been included in this submission.

Conflicts of interest

The authors declare no conflict of interest.

References

1 O. C. Olatunde, L. Sawunyama, T. L. Yusuf and D. C. Onwudiwe, *J. Water Process Eng.*, 2024, **66**, 105890.
2 T. L. Yusuf, B. O. Orimolade, D. Masekela, B. Mamba and N. Mabuba, *RSC Adv.*, 2022, **12**, 26176–26191.
3 D. Yadav, S. Rangabhashiyam, P. Verma, P. Singh, P. Devi, P. Kumar, C. M. Hussain, G. K. Gaurav and K. S. Kumar, *Chemosphere*, 2021, **272**, 129492.
4 X. Hu, X. Hu, Q. Peng, L. Zhou, X. Tan, L. Jiang, C. Tang, H. Wang, S. Liu and Y. Wang, *Chem. Eng. J.*, 2020, **380**, 122366.
5 E. O. Omotola, A. O. Oluwole, P. O. Oladoye and O. S. Olatunji, *Environ. Toxicol. Pharmacol.*, 2022, **91**, 103831.
6 T. L. Yusuf, O. C. Olatunde, D. Masekela, N. Mabuba, D. C. Onwudiwe and S. Makgato, *Ceram. Int.*, 2024, **50**, 45581–45591.

7 T. An, H. Yang, G. Li, W. Song, W. J. Cooper and X. Nie, *Appl. Catal., B*, 2010, **94**, 288–294.
8 X. Nie, X. Wang, J. Chen, V. Zitko and T. An, *Environ. Toxicol. Chem.*, 2008, **27**, 168–173.
9 T. L. Yusuf, B. O. Ojo, T. Mushiana, N. Mabuba, O. A. Arotiba and S. Makgato, *Catal. Sci. Technol.*, 2024, **14**, 6015–6026.
10 R. Nejat, *Heliyon*, 2024, **10**(16), e35829.
11 T. L. Yusuf, O. C. Olatunde, D. Masekela, K. D. Modibane, D. C. Onwudiwe and S. Makgato, *ChemElectroChem*, 2024, **11**, e202400309.
12 F. Chen, Q. Yang, X. Li, G. Zeng, D. Wang, C. Niu, J. Zhao, H. An, T. Xie and Y. Deng, *Appl. Catal., B*, 2017, **200**, 330–342.
13 B. Y. Balarabe, P. Maity, A. C. S. Teixeira and S. A. Iwarere, *Inorg. Chem. Commun.*, 2023, **158**, 111560.
14 P. Alfonso-Muniozguren, E. A. Serna-Galvis, M. Bussemaker, R. A. Torres-Palma and J. Lee, *Ultrason. Sonochem.*, 2021, **76**, 105656.
15 S. K. Tammina, B. K. Mandal and F. N. Khan, *Environ. Technol.*, 2019, **13**, 197–210.
16 S. A. Bhat, F. Zafar, A. H. Mondal, A. Kareem, A. U. Mirza, S. Khan, A. Mohammad, Q. M. R. Haq and N. Nishat, *J. Iran. Chem. Soc.*, 2020, **17**, 215–227.
17 I. El Saliby, L. Erdei, J.-H. Kim and H. K. Shon, *Water Res.*, 2013, **47**, 4115–4125.
18 H. A. A. Jamjoum, K. Umar, R. Adnan, M. R. Razali and M. N. Mohamad Ibrahim, *Front. Chem.*, 2021, **9**, 752276.
19 D. Masekela, N. C. Hintsho-Mbita, L. N. Dlamini, T. L. Yusuf and N. Mabuba, *Mater. Today Commun.*, 2024, **38**, 108500.
20 J. Luo, K. Wang, Y. Qiu, X. Zhou, X. Ning, L. Zhan and X. Zhou, *J. Alloys Compd.*, 2024, **1008**, 176572.
21 L. Zhong, L. Chen, X. Xie, Z. Qin and T. Su, *Catalysts*, 2024, **14**, 722.
22 T. L. Yusuf, S. A. Ogundare, F. Opoku, O. A. Arotiba and N. Mabuba, *J. Environ. Chem. Eng.*, 2023, **11**, 110711.
23 T. L. Yusuf, S. A. Ogundare, F. Opoku and N. Mabuba, *Surf. Interfaces*, 2023, **36**, 102534.
24 O. Monfort and G. Plesch, *Environ. Sci. Pollut. Res.*, 2018, **25**, 19362–19379.
25 J. Silva, N. A. Neto, M. Teodoro, A. Paiva, M. Bomio and F. Motta, *J. Alloys Compd.*, 2022, **928**, 167136.
26 B. Shanthi, K. Saravanan, C. Ravichandran, B. Venkatachalapathy, K. Sathiyanarayanan, N. Karthikeyan and R. Suresh, *Mater. Lett.*, 2023, **351**, 135010.
27 A. Nagar and S. Basu, *Environ. Technol.*, 2021, **23**, 101646.
28 A. Yousefi, A. Nezamzadeh-Ejhieh and M. Mirmohammadi, *Environ. Technol.*, 2021, **22**, 101496.
29 A. Yousefi, A. Nezamzadeh-Ejhieh and M. Mirmohammadi, *Environ. Technol.*, 2021, **22**, 101433.
30 M. Liang, Y. Yu, Y. Wang and Y. Yu, *J. Hazard. Mater.*, 2020, **391**, 121016.
31 K. Wangkawong, W. Lanla, V. Supphachalonepol, D. Channei and B. Inceesungvorn, *Inorg. Chem. Commun.*, 2024, 112260.
32 Y. Lin, R. Hong, H. Chen, D. Zhang and J. Xu, *J. Nanomater.*, 2020, **2020**, 4147357.
33 O. H. Abuzeyad, A. M. El-Khawaga, H. Tantawy and M. A. Elsayed, *J. Mol. Struct.*, 2023, 135787.
34 X. Yu, J. Shi, L. Feng, C. Li and L. Wang, *Appl. Surf. Sci.*, 2017, **396**, 1775–1782.
35 S. Phanichphant, A. Nakaruk, K. Chansaenpak and D. Channei, *Sci. Rep.*, 2019, **9**, 16091.
36 M. Piao, Y. Sun, Y. Wang and H. Teng, *ChemistrySelect*, 2022, **7**, e202200182.
37 J. Chen, B. Yao, C. Li and G. Shi, *Carbon*, 2013, **64**, 225–229.
38 T. Mohlala, T. L. Yusuf and N. Mabuba, *J. Electroanal. Chem.*, 2023, **947**, 117806.
39 L. Yi, H. Jiang, Y. Ma, R. Zhu, G. Zhang and Z. Ren, *Chemosphere*, 2024, **354**, 141658.
40 N. Rajalakshmi, D. Barathi, S. Meyvel and P. Sathya, *Inorg. Chem. Commun.*, 2021, **132**, 108849.
41 O. A. Oyewo, S. Ramaila and L. Mavuru, *Inorg. Chem. Commun.*, 2023, **151**, 110601.
42 S. Mansour, R. Akkari, S. Ben Chaabene and M. Saïd Zina, *Adv. Mater. Sci. Eng.*, 2020, **2020**, 6505301.
43 O. Oyegbeda, S. O. Akpotu and B. Moodley, *J. Environ. Chem. Eng.*, 2024, 113447.
44 R. Li, F. Zhang, D. Wang, J. Yang, M. Li, J. Zhu, X. Zhou, H. Han and C. Li, *Nat. Commun.*, 2013, **4**, 1432.
45 C. V. Reddy, A. Nagar, N. P. Shetti, I. N. Reddy, S. Basu, J. Shim and R. R. Kakarla, *Chemosphere*, 2023, **322**, 138146.
46 Y. Wang, J. Sun, J. Li and X. Zhao, *Langmuir*, 2017, **33**, 4694–4701.
47 S. Chen, D. Huang, G. Zeng, W. Xue, L. Lei, P. Xu, R. Deng, J. Li and M. Cheng, *Chem. Eng. J.*, 2020, **382**, 122840.
48 R. Kanagadurai, R. Sankar, G. Sivanesan, S. Srinivasan, R. Rajasekaran and R. Jayavel, *Mater. Chem. Phys.*, 2008, **108**, 170–175.
49 A. Malathy, V. Manikandan, S. Devanesan, K. Farhat, A. Priyadharsan, C. Ragavendran, S. Ragupathy, R. Ranjith and S. Sivakumar, *Int. J. Biol. Macromol.*, 2023, **244**, 125303.
50 A. O. Oluwole and O. S. Olatunji, *Chem. Eng. J. Adv.*, 2022, **12**, 100417.
51 P. Madhusudan, J. Ran, J. Zhang, J. Yu and G. Liu, *Appl. Catal., B*, 2011, **110**, 286–295.
52 B. O. Orimolade and O. A. Arotiba, *Sci. Rep.*, 2020, **10**, 5348.
53 L. Zhang, Z. Dai, G. Zheng, Z. Yao and J. Mu, *RSC Adv.*, 2018, **8**, 10654–10664.
54 A. N. Zulkifili, A. Fujiki and S. Kimijima, *Appl. Sci.*, 2018, **8**, 216.
55 H. Li, Y. Sun, B. Cai, S. Gan, D. Han, L. Niu and T. Wu, *Appl. Catal., B*, 2015, **170**, 206–214.
56 A. Raja, P. Rajasekaran, K. Selvakumar, M. Arunpandian, K. Kaviyarasu, S. A. Bahadur and M. Swaminathan, *Sep. Purif. Technol.*, 2020, **233**, 115996.
57 A. V. Karim and A. Shriwastav, *Chem. Eng. J.*, 2020, **392**, 124853.
58 E. Cristiano, Y.-J. Hu, M. Sigfried, D. Kaplan and H. Nitsche, *Clays Clay Miner.*, 2011, **59**, 107–115.
59 A. Hassani, A. Khataee and S. Karaca, *J. Mol. Catal. A: Chem.*, 2015, **409**, 149–161.
60 W. D. Santos, M. M. Teixeira, I. R. Campos, R. B. de Lima, A. Mantilla, J. A. Osajima, A. S. de Menezes, D. Manzani, A. Rojas and A. C. Alcântara, *Microporous Mesoporous Mater.*, 2023, **359**, 112657.

61 J. Liu, L. Zhang, Y. Sun and Y. Luo, *Nanomaterials*, 2021, **11**, 1104.
62 M. Joy, B. N. Nair, A. A. P. Mohamed, K. G. Warrier and U. N. S. Hareesh, *Eur. J. Inorg. Chem.*, 2016, 3912–3920.
63 R. A. Senthil, S. Osman, J. Pan, A. Khan, V. Yang, T. R. Kumar, Y. Sun, Y. Lin, X. Liu and A. Manikandan, *Colloids Surf., A*, 2020, **586**, 124079.
64 A. O. Oluwole and O. S. Olatunji, *J. Water Process Eng.*, 2023, **54**, 104045.
65 M. Pirhashemi, S. Elhag, R. E. Adam, A. Habibi-Yangjeh, X. Liu, M. Willander and O. Nur, *RSC Adv.*, 2019, **9**, 7992–8001.
66 H. Zhang, H. Azimi, M. Mahmoudian, M. Ebadi, R. Moradi, A. Shirmardi and R. Yousefi, *J. Environ. Manage.*, 2024, **370**, 122734.